

# Diurnal Thermal Cycling Effects on Microwave Signatures of Thin Sea Ice

Son V. Nghiem, *Member, IEEE*, Ronald Kwok, *Member, IEEE*, Simon H. Yueh, *Member, IEEE*,  
Anthony J. Gow, Donald K. Perovich, Chih-Chien Hsu, Kung-Hau Ding,  
Jin Au Kong, *Fellow, IEEE*, and Thomas C. Grenfell, *Member, IEEE*

**Abstract**—To investigate effects of diurnal thermal cycles on C-band polarimetric backscatter and millimeter-wave emission from sea ice, we carried out a winter experiment at the outdoor Geophysical Research Facility (GRF) in the Cold Regions Research and Engineering Laboratory (CRREL). The ice sheet grew from open sea water to a thickness of 10 cm in 2.5 days, during which we took polarimetric backscatter data with a C-band scatterometer, interlaced with brightness temperature measurements at 90 GHz in conjunction with meteorological and sea ice characterizations. The initial ice growth in the late morning was slow due to high insolation. As the air temperature dropped during the night, the growth rate increased significantly. Air temperature changed drastically from about  $-12$  to  $-36$  °C between day and night. The diurnal thermal cycle repeated itself the next day and the growth rate varied in the same manner. Ice temperature profiles clearly show the diurnal response in the ice sheet with a lag of 2.5 h behind the time of the maximum short-wave incident solar radiation. The diurnal cycles are also evident in the millimeter-wave brightness temperature data. Measured sea ice backscatter revealed substantial diurnal variations up to 6 dB with repeatable cycles in synchronization with the temperature cycles and the brightness temperature modulations. The diurnal cycles in backscatter indicate that the dominant scattering mechanism related to thermodynamic processes in sea ice is reversible. A diurnal backscatter model based on sea ice electrodynamics and thermodynamics explains the observed diurnal signature. This work shows that diurnal effects are important for inversion algorithms to retrieve sea ice geophysical parameters from remote sensing data acquired with a satellite synthetic aperture radar (SAR) or scatterometer on sun-synchronous orbits.

**Index Terms**—Backscatter, brightness temperature, diurnal thermal cycle, sea ice.

Manuscript received September 27, 1996; revised May 14, 1997. This work was performed at the Center for Space Microelectronics Technology, Jet Propulsion Laboratory, California Institute of Technology, Pasadena, CA, and was sponsored by the Office of Naval Research (ONR) through an agreement with the National Aeronautics and Space Administration. Participations by the U.S. Army CRREL was supported by ONR Contracts N00014-95-MP-3002 and N00014-95-MP-3019, by the Massachusetts Institute of Technology under ONR Contracts N00014-89-J-1107 and N00014-92-J-4098, and by the University of Washington under ONR Contracts N00014-89-J-1140 and N00014-89-J-3132.

S. V. Nghiem, R. Kwok, and S. H. Yueh are with the Center for Space Microelectronics Technology, Jet Propulsion Laboratory, California Institute of Technology, Pasadena, CA 91109 USA (e-mail: nghiem@solar.jpl.nasa.gov; simon@malibu.jpl.nasa.gov).

A. J. Gow and D. K. Perovich are with the U.S. Army Cold Regions Research and Engineering Laboratory, Hanover, NH 03755 USA.

C.-C. Hsu, K.-H. Ding, and J. A. Kong are with the Department of Electrical Engineering and Computer Science and Research, Laboratory of Electronics, Massachusetts Institute of Technology, Cambridge, MA 02139 USA.

T. C. Grenfell is with the Department of Atmospheric Sciences, University of Washington, Seattle, WA 98195 USA.

Publisher Item Identifier S 0196-2892(98)00548-8.

## I. INTRODUCTION

LEADS containing thin ice in the perennial sea ice pack contribute significantly to the heat transfer between the Arctic Ocean and the atmosphere [1], [2]. By triggering fog and clouds, leads affect the net radiative transfer balance [3]. Leads impact the thermohaline structure of the upper Arctic Ocean despite their small areal coverage relative to other sea ice types. In active leads, salt released by rapid freezing mixes downward by turbulence [4]. From the Leads Experiment conducted in March and April 1992 on the Arctic ice pack about 200 km north of Prudhoe Bay [5], Ruffieux *et al.* [3] found that the sun was effective in reducing the surface freezing rate of lead ice formation and in halting the convective mixing in the ocean under the leads. They concluded that downward short-wave radiation was responsible for driving the diurnal cycles [3]. During the same experiment, McPhee and Stanton [4] observed large downward oceanic heat flux near solar noon in the diurnal cycle of warming and cooling of the mixed layer.

With spaceborne infrared cloud-free surface-temperature images, Ikeda [6] demonstrated a diurnal effect on sea ice, which appeared brighter in nighttime images than in daytime images. Using airborne X-band synthetic aperture radar (SAR) images, Barber *et al.* [7] reported diurnal differences in multi-year ice and in a rubble field seen at two different times in the Canadian Arctic Archipelago. These results, however, did not include diurnal observations of thin sea ice in active leads. Sparse temporal observations also limit the utility of satellite data to investigate the diurnal signatures of sea ice in remote sensing data and their relation to diurnal responses in sea ice physical properties [6]. Yet understanding the physical mechanisms responsible for observed diurnal signatures is necessary for correctly interpreting and retrieving geophysical parameters from remote sensing data.

The objective of the present work is to investigate the diurnal signature in C-band polarimetric backscatter together with millimeter-wave emission of thin sea ice in active leads. We study the linkage between the diurnal microwave signatures and sea ice physical properties undergoing cyclic cooling and warming driven by the insolation. Furthermore, an important and practical purpose is to determine whether diurnal effects are necessary for algorithms using microwave remote sensing data to retrieve geophysical parameters such as sea ice thickness [8]. The C-band polarimetric results are of particular interest because many current and planned spaceborne SAR's

and scatterometers such as ERS, RADARSAT, and ENVISAT operate at C band with different polarizations.

In this paper, we present observations on C-band polarimetric backscatter and millimeter-wave dual-polarization brightness temperatures of sea ice growing under diurnal cycling conditions. We conducted the experiment at the outdoor Geophysical Research Facility (GRF) in the Cold Regions Research and Engineering Laboratory (CRREL) from January 19–21, 1994, during which an ice sheet was grown to a thickness of 10 cm. This thickness was in the same range of the diurnal study by Ruffieux *et al.* [3] in LeadEx, which emphasized leads covered with thin ice during the first few days of their life cycles. The meteorological environment prevailing at the time of our experiment was particularly suitable for studying effects of diurnal variations. Air temperature plunged down to Arctic values ( $-36^{\circ}\text{C}$ ), the temperature change between day and night was more than  $20^{\circ}\text{C}$ , and the mostly clear sky allowed strong insolation. We used the Jet Propulsion Laboratory (JPL) C-band polarimetric scatterometer to take backscatter data in conjunction with meteorological, sea ice characterization, and brightness temperature measurements taken with a 90 GHz radiometer from the University of Washington (UW).

## II. DESCRIPTIONS OF THE EXPERIMENT

### A. Facility

The ice sheet grew in the GRF pond filled with sea water of 30 ppt salinity. The pond was 18.3 m long, 7.62 m wide, and 2.14-m deep as shown in Fig. 1. A gantry, movable on rails along the pond, provided the support to mount the C-band polarimetric scatterometer at about 4 m above the surface of the ice sheet (we will describe the scatterometer later in Section II-B). A heated tent near one corner of the pond provided a warm environment for the observers and the scatterometer controller. At the other corner on the same side of the pond (see Fig. 1), there was a small pump house where the controlling computer for acquiring temperature profiles of the ice sheet was located. A concrete walkway connected the tent and the pump house, where we set up a site for calibration targets.

We used a 90-GHz radiometer, mounted on a movable framework attached to the rail of the pond, to measure brightness temperature at various sites along the entire length of the pond. For local environmental conditions, we made use of data collected at the CRREL meteorological station for short-wave and long-wave radiation, air temperature, wind speed, and wind direction [9]. To determine crystallographic structures of sea ice, we prepared horizontal and vertical thin sections of ice samples in a CRREL refrigerated room for a three-dimensional examination of the structures. Two thermistor strings, suspended in the sea water prior to freezing, gave temperature profiles of the sea ice and sea water as a function of time during the experiment.

### B. Experimental Setup

The scatterometer was a step-frequency radar with the center frequency of 5 GHz, a bandwidth of 1 GHz, and a

beamwidth of  $12^{\circ}$ . Fig. 2 shows the scatterometer antenna with the positioner mounted on the gantry I-beams. The antenna was a dual polarization diagonal horn installed on a square frame, which we rotated around a horizontal axis with a remote-controlled motor to set the incident angle. In Fig. 2, the antenna was at the position of normal incidence or  $0^{\circ}$  incident angle. The entire antenna fixture was bolted on a ball bearing disk driven with another remote controlled motor to change the azimuth angle.

The insulated white box close to the antenna seen in the photo contains RF electronic components, which were kept at a constant temperature of  $25^{\circ}\text{C}$  throughout the experiment. The scatterometer computer and controllers together with the network analyzer were in the tent, from which we operated the scatterometer. Detailed descriptions of the scatterometer system, antenna characteristics, operation, sensitivity, calibration, and data processor have been presented elsewhere [10], [11].

For this experiment, we arranged calibration targets on a styrofoam pedestal placed on top of a cardboard box at the calibration site indicated in Fig. 1. The calibration targets were a trihedral corner reflector and a metallic sphere. We covered the front of the box and the background of the calibration target with microwave absorber sheets to reduce noise. The coherent subtraction technique was applied to obtain excellent calibration data. We regularly made clear sky measurements to determine system noises for removal from calibration and sea ice measurements.

The 90-GHz radiometer was located on the east side of the pond across from the scatterometer calibration site as shown in Fig. 1. The radiometer was a noise-injection Dicke type with a bandwidth of 500 MHz and a field-of-view of  $6^{\circ}$  using a horn lens antenna with a 92% efficiency in the main lobe. The height of the radiometer antenna was approximately 1.5 m above the surface of the ice sheet. This radiometer was designed for surface-based measurements of thermal microwave emission from sea ice in Arctic field conditions. Further details have been presented by Grenfell and Lohanick [12].

A station, situated on an elevated terrain about 7.3 m above and 183 m away from the GRF pond, monitored basic meteorological data. We also took sea ice samples prior to each set of backscatter measurements to measure ice thickness, salinity, and structure. We set the thermistor strings vertically in the ice directly in front of the pump house and away from the microwave study areas for all incident and azimuth angles. Additionally, we used hand-held digital thermometers to take air and ice surface temperatures at the other end of the pond.

### C. Data Collection

For approximately every 1 cm of the ice growth, we took a set of polarimetric backscatter data with an increment of  $5^{\circ}$  over the incident angle range. At every incident angle, we measured full scattering matrices for three independent azimuth angles. Each scattering matrix was a coherent average of 20 samples with 401 frequency points over 1 GHz bandwidth. The data processing [10], [11] included data decompression, system noise removal, windowing, Fourier transforms, time gating, system transfer function computation, signal re-

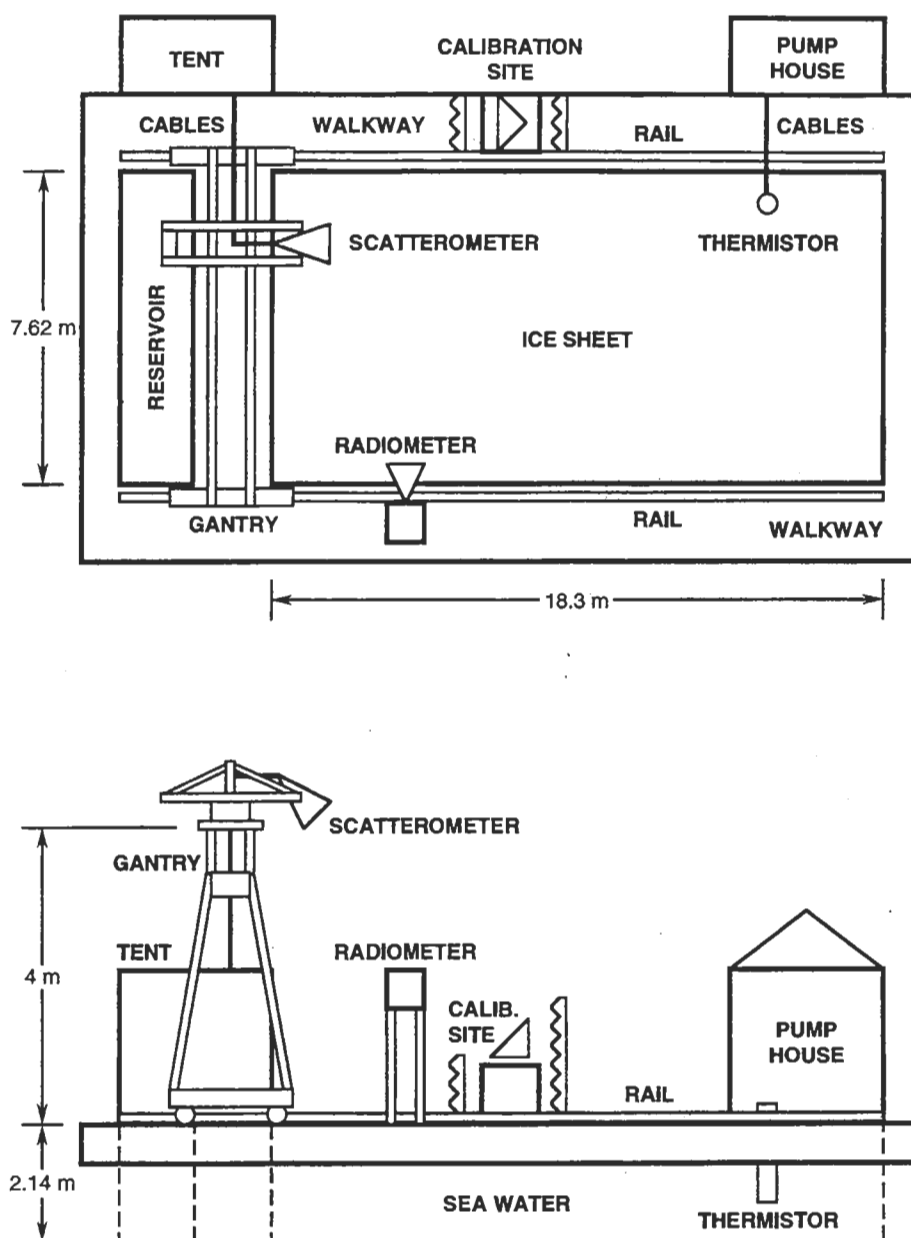


Fig. 1. Experimental setup at the Geophysical Research Facility in the Cold Regions Research and Engineering Laboratory. This diagram is not drawn to scale.

construction, ensemble averaging, three-dimensional antenna pattern characterization, backscatter deconvolution, and polarimetric and radiometric calibrations. Processed backscatter data consisted of  $\sigma_{hh}$  for horizontal polarization,  $\sigma_{vv}$  for vertical polarization,  $\sigma_{hv}$  for cross-polarization, and  $\rho$  for complex correlation between horizontal and vertical returns.

We interlaced sets of scatterometer and radiometer measurements. In this approach, we completed a set of scatterometer measurements, then took the radiometer data, and repeated the procedure for each growth stage. This data acquisition arrangement prevented scatterometer interferences in microwave brightness temperature observations. The response time of the ice sheet characteristics to environmental conditions was much slower than the time interval between the interlaced scatterometer and radiometer measurements. Hence, sea ice

properties were similar between the two sets of observations for the same growth stage. Brightness temperatures of the ice sheet for both horizontal and vertical polarizations were at an incident angle of  $50^\circ$ . We chose this angle to correspond to the incident angle of the SMMR and SSM/I satellite sensors. The accuracy in brightness temperature was about 2 K with a sensitivity of 0.5 K.

The meteorological station was equipped with sensors for measuring air temperature, short-wave and long-wave radiations, wind speed, and wind direction. For air temperature, a Rotronics MP-100 Probe took data and averaged measurements over 15 min with a precision of  $0.1^\circ\text{C}$ . The sensors for radiation were a short-wave Qualimetrics 3020 Starpyranometer ( $0.3\text{--}3\ \mu\text{m}$ ) and a long-wave Eppley Pyrgeometer ( $3\text{--}50\ \mu\text{m}$ ). The wind monitor was an RM Young model 5103 which

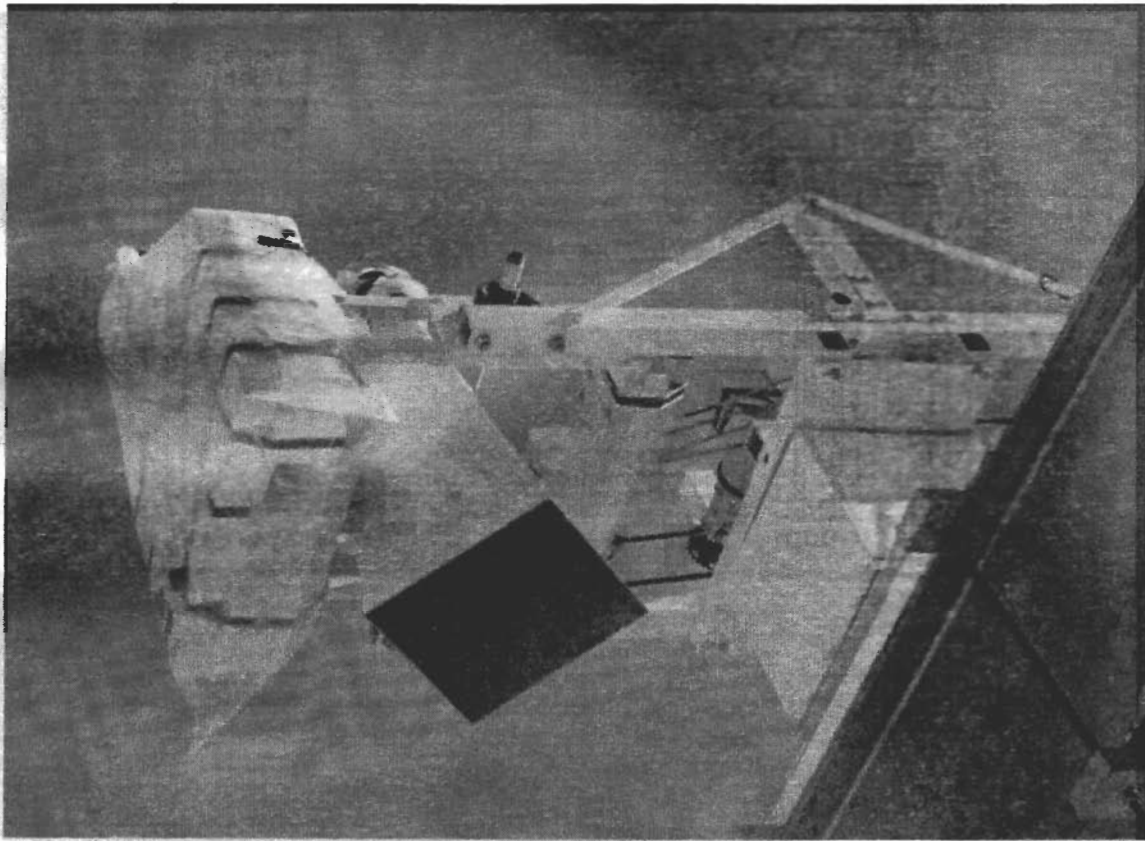


Fig. 2. Photograph of the JPL C-band scatterometer antenna mounted on the positioner together with the RF box. The whole fixture was bolted on the double I-beams above the GRF pond at CRREL.

measured both wind speed and wind direction. The CRREL Meteorological Team reported additional information on the sensors and data collection [9].

We used the two thermistor strings to monitor the vertical profile of temperature in sea ice and sea water. The strings consisted of YSI-44033 precision thermistors mounted in solid 3.2-cm diameter PVC rods. The spacing of the thermistors was every 0.5 cm in the top 7 cm, every 1 cm from 7 to 18 cm, and every 5 cm from 18 to 48 cm. A Campbell Scientific data logger recorded temperature profile data every 5 min. The thermistors had an absolute accuracy of 0.1 °C and a sensitivity of approximately 0.03 °C.

### III. SEA ICE GROWTH

#### A. Environment

In a typical midlatitude winter, the amplitude of the diurnal cycle of solar radiation is similar to the Arctic condition in late winter to early spring, such as the LeadEx March–April time frame [3]. The peak incident short-wave radiation is well above  $400 \text{ W} \cdot \text{m}^{-2}$  at solar noon. This strong insolation drives the diurnal thermal cycling which causes physical changes in sea ice properties. The top panel of Fig. 3 shows integrated values of incident radiation for both short-wave ( $0.3\text{--}3 \mu\text{m}$ ) and atmospheric long-wave ( $3\text{--}50 \mu\text{m}$ ) regimes measured at the meteorological station from January 19–22, 1994. The short-wave peak occurred close to local noon and the amplitude was typical of local winter values. On January 21, some cloudiness was present, which reduced the downward short-

wave irradiance. The long-wave radiation was between 200 to  $300 \text{ W} \cdot \text{m}^{-2}$ , decreasing from maximum values in the late afternoon to minimum values in the early morning.

Air temperatures lagged the incident short-wave radiation as seen in the bottom panel of Fig. 3. Temperatures measured at the station were in close agreement with those measured at the GRF. The temperature peak was approximately 2.5 h offset from the short-wave peak. Fig. 3 indicates that solar heating caused the steep slope in the temperature curve during noon time. After the sunset, the temperature gradually cooled down throughout the night. The minimum nighttime air temperature was  $-36 \text{ °C}$ , which is similar to Arctic early spring conditions. The winter of 1994, in New Hampshire, was one of the coldest ever recorded. During the experiment, the temperature varied more than  $20 \text{ °C}$  from day to night. Arctic measurements in early spring also show a substantial heating during the day and cooling during the night [3].

High winds can be an important factor in the surface energy balance influencing the ice growth [13]. It is desirable to have a persistent or low wind condition to avoid complicated variations in the ice growth process. Over the duration of our experiment, the average wind speed measured at the meteorological station was quite small—only  $0.6 \text{ m} \cdot \text{s}^{-1}$  at 4 m height above the station ground level in addition to 7.3 m above the GRF pond. Since the GRF pond was in the middle of a terrain depression surrounded by elevated hill sides, buildings, and fences, wind speeds at the experiment site were even lower or essentially close to the still air condition. These

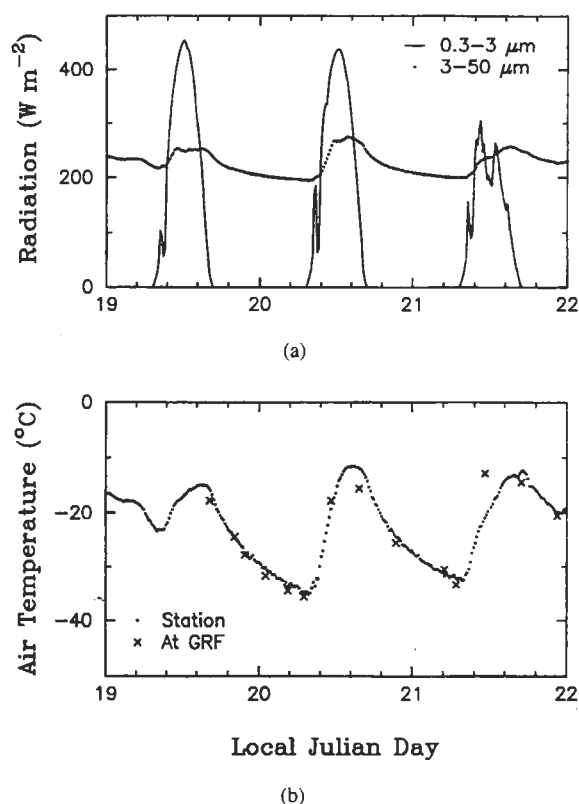


Fig. 3. Meteorological conditions: (a) the top panel shows short-wave radiation from 0.3 to 3  $\mu\text{m}$  with the continuous curve and long-wave incident radiation from 3 to 50  $\mu\text{m}$  with the dotted curve and (b) the bottom panel is air temperature measured at the meteorological station with the dotted curve and at the GRF pond with the crosses.

environmental conditions encountered during this experiment were particularly suitable to study the diurnal backscatter signature of thin sea ice similar to that forming in Arctic leads under quiescent conditions.

### B. Growth Process

We initiated the ice growth from open saline water at about 10:00 AM local time on January 19, 1994. The water had a salt mixture very close to that of natural sea water in the Arctic Ocean and consisted of mainly sodium chloride ( $\text{NaCl}$ , 23.98  $\text{kg} \cdot \text{m}^{-3}$ ), magnesium chloride ( $\text{MgCl}_2$ , 3.7  $\text{kg} \cdot \text{m}^{-3}$ ), magnesium sulfate ( $\text{MgSO}_4$ , 1.50  $\text{kg} \cdot \text{m}^{-3}$ ), calcium sulfate ( $\text{CaSO}_4$ , 1.10  $\text{kg} \cdot \text{m}^{-3}$ ), potassium sulfate ( $\text{K}_2\text{SO}_4$ , 0.70  $\text{kg} \cdot \text{m}^{-3}$ ), and calcium carbonate ( $\text{CaCO}_3$ , 0.10  $\text{kg} \cdot \text{m}^{-3}$ ). We selected the salt concentrations to produce a salinity of 30 ppt. This mixture contains the same salt fractions as in typical sea water [14] excluding trace amounts of potassium bromide ( $\text{KBr}$ ), strontium sulfate ( $\text{SrSO}_4$ ), and boric acid ( $\text{H}_3\text{BO}_3$ ). Together these account for a negligible salinity of 0.1 ppt.

The top panel of Fig. 4 shows the temperature profiles (A–E) measured *in situ* with the thermistor system from 0.2 cm below the ice surface to a depth of 8.2 cm at 2-cm intervals. The temperature records started at the time of the initial ice growth. The air temperature measured by the meteorological station is also replotted for reference. From these results, the time constant of the interfacial and subsurface thermal response is about 2.5 h corresponding to the time lag

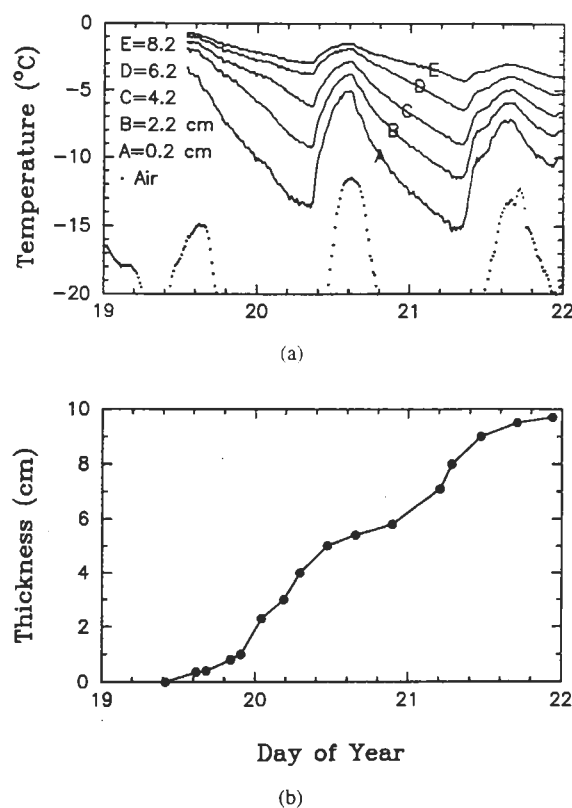


Fig. 4. Diurnal response in temperature of the sea ice sheet growing under warming and cooling cycles: (a) temperature profiles of the sea ice and sea water are represented by continuous curves at depths A = 0.2 cm, B = 2.2 cm, C = 4.2 cm, D = 6.2 cm, and E = 8.2 cm, and the dotted curve is air temperature measured at the nearby meteorological station; and (b) change in sea ice thickness over 2.5 days with two diurnal cycles, the data are represented by dots connected with the continuous line.

between the temperature peaks and the maximum short-wave insolation (compare top panels of Figs. 3 and 4). A closer examination of the temperature extrema indicates a slightly slower response deeper in the ice. At a depth closer to the ice-water interface, the temperature peak-to-peak variation in the ice layer was significantly smaller. These observations indicate that the insolation was driving the diurnal thermal cycles.

Since sea ice growth rate depends on the temperature difference between air and water [14], [15], diurnal cooling and warming directly influence the ice growth. The bottom panel of Fig. 4 presents the sea ice growth up to 10 cm in thickness during the 2.5 days of the experiment. The result shows a clear slowdown in the ice growth corresponding to the daytime warming of the ice sheet. In effect, the solar input tends to shut off the growth and consequently halts the salt rejection into the sea water. A comparison of these results and Arctic field observations [3], [4] shows that the Arctic diurnal thermal responses also have definitive afternoon peaks but with a broader time width due to the longer insolation interval in the Arctic. In both cases, diurnal thermal cycling effects are pronounced and have similar trends.

### C. Physical Characteristics

At the time of the initial growth, the solar short-wave radiation was high (top panel, Fig. 3) and the growth rate was

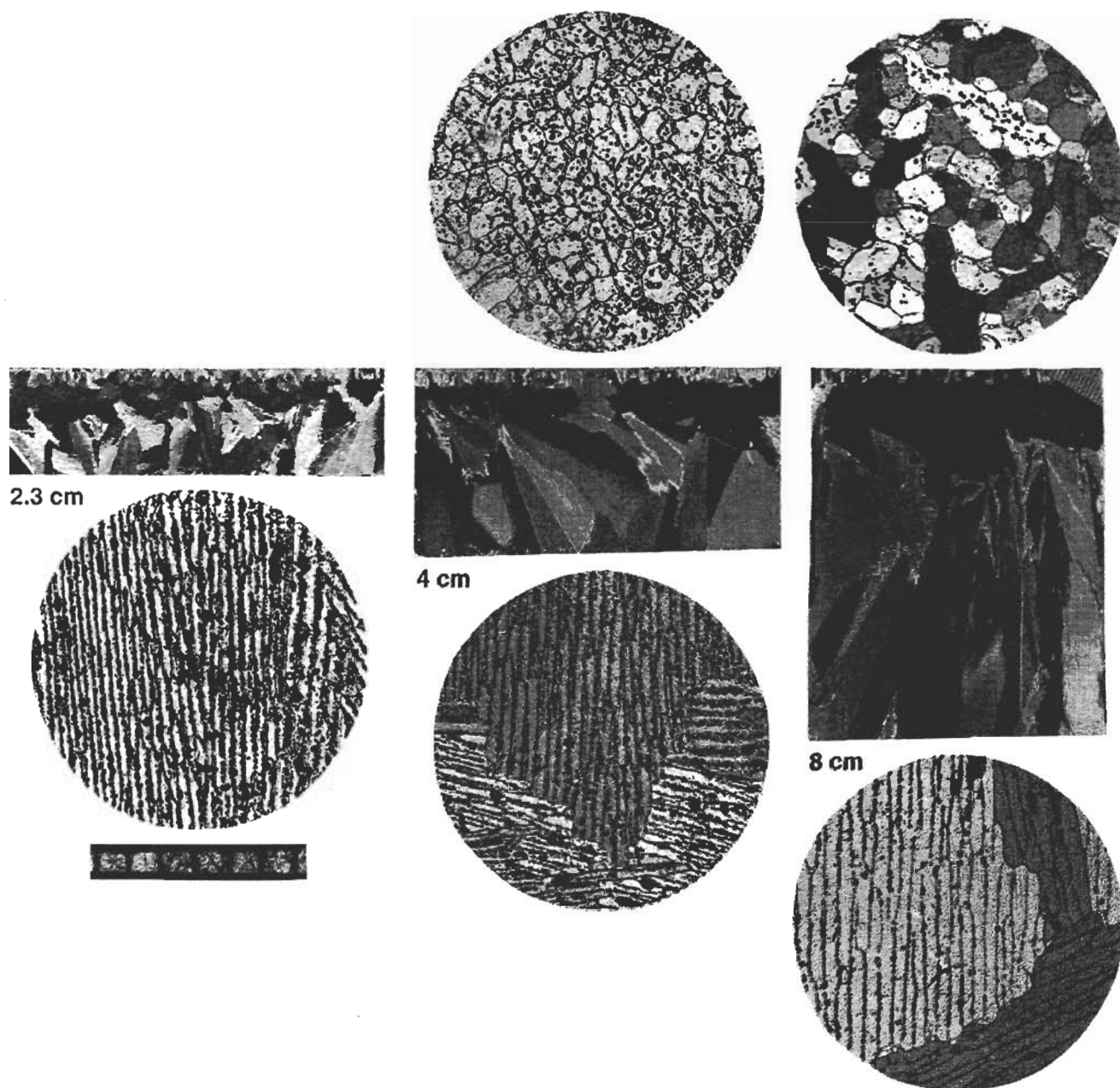


Fig. 5. Horizontal and vertical thin sections of sea ice for several growth stages at thicknesses of (a) 2.3 cm, (b) 4.0 cm, and (c) 8.0 cm. The millimeter bar under the horizontal thin section of the 2.3-cm ice sample represents the scale for all horizontal thin sections. The ruler with millimeter marking on the top right corner of the 8-cm vertical thin section is the scale for all vertical thin sections. The incubation layer is evident at the top 2–4 mm of every vertical thin section.

very slow (bottom panel, Fig. 4). This slow growth produced a thin incubation layer consisting of 2–4 mm of granular ice with vertical crystallographic  $c$  axes and a low salinity. The formation of the incubation layer had been observed on urea ice in laboratory conditions [16] and on natural sea ice in the Bay of Bothnia [17]. This initial layer occupied the top few millimeters as seen in the vertical thin sections in Fig. 5. Below the incubation layer, ice crystals made the transition to ordinary columnar sea ice with  $c$  axes tilted away from nadir and randomly oriented in the azimuth. Comparing the top and the bottom horizontal thin sections in Fig. 5, we observe the contrast between the granular nature of ice in the incubation layer and the typical ice plate and brine layer substructure of columnar ice.

Fig. 6 presents salinity profiles of sea ice samples at various growth stages with different thicknesses. The salinity profiles indicate that the near-surface incubation layer contained significantly lower salinity in all cases. This is consistent with the formation of the incubation layer at a very low growth rate around solar noon on January 19. A slow growth rate results in more effective brine rejection and consequently less brine entrapment in sea ice [18], [19]. Also apparent is the progressive loss of brine as the ice sheet thickens below about 3 cm.

The brine loss or desalination is also seen in the decrease of bulk salinity for thicker ice as shown in the top panel of Fig. 7. The linear fitted curve has an initial value of 12.0 ppt and a negative slope of 0.458 ppt/cm. The internal



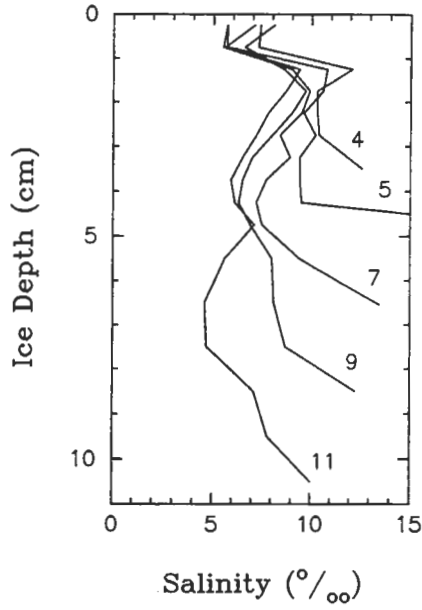


Fig. 6. Salinity profiles for several growth stages at thicknesses of 4, 5, 7, 9, and 11 cm. The near-surface ice layer has low salinity in all cases indicating the existence of the incubation layer.

salinity loss was primarily by downward brine flux because the incubation layer hindered the upward brine expulsion and migration. Average ice temperatures, obtained by integrating the ice temperature profiles and normalizing over the thickness of the ice sheet, also show the diurnal cycles with high daytime values corresponding to thicknesses of about 0.5, 5, and 10 cm, as seen in the middle panel of Fig. 7. For each cycle, a quadratic function fits the temperature data and is plotted with the continuous curve.

The bottom panel of Fig. 7 shows variations in brine volume versus ice thickness. The filled circles represent calculations from thermodynamic phase equations of Cox and Weeks [20] based on measured or extrapolated salinities and temperatures. The brine volume curve is from fitted salinity and temperature values. A combination of desalination and diurnal effects are both manifest in the brine volume over the 10-cm range of thickness with a general decreasing trend imposed on the thermal cycles. The diurnal cycles in the brine volume are quite significant with a nighttime freeze-up of 50% liquid phase and a daytime recovery of 50% brine volume observed in both cycles.

Brightness temperatures of the ice sheet for both horizontal and vertical polarizations  $T_{Bh}$  and  $T_{Bv}$ , respectively, at 90 GHz and  $50^\circ$  incident angle show diurnal cycles as seen in Fig. 8. The cycles are well defined except for the first few millimeters of the ice growth when the phase transition was inhomogeneous and complicated. Note that the daytime peak at the growth stage between 5 and 6 cm coincides with the ice temperature peak in Fig. 7 and with the surface temperature peak replotted as a function of ice thickness in Fig. 9. This is because brightness temperatures are sensitive to the physical temperature of the target. Fig. 8 also shows that peak-to-peak variations of the diurnal cycles in brightness

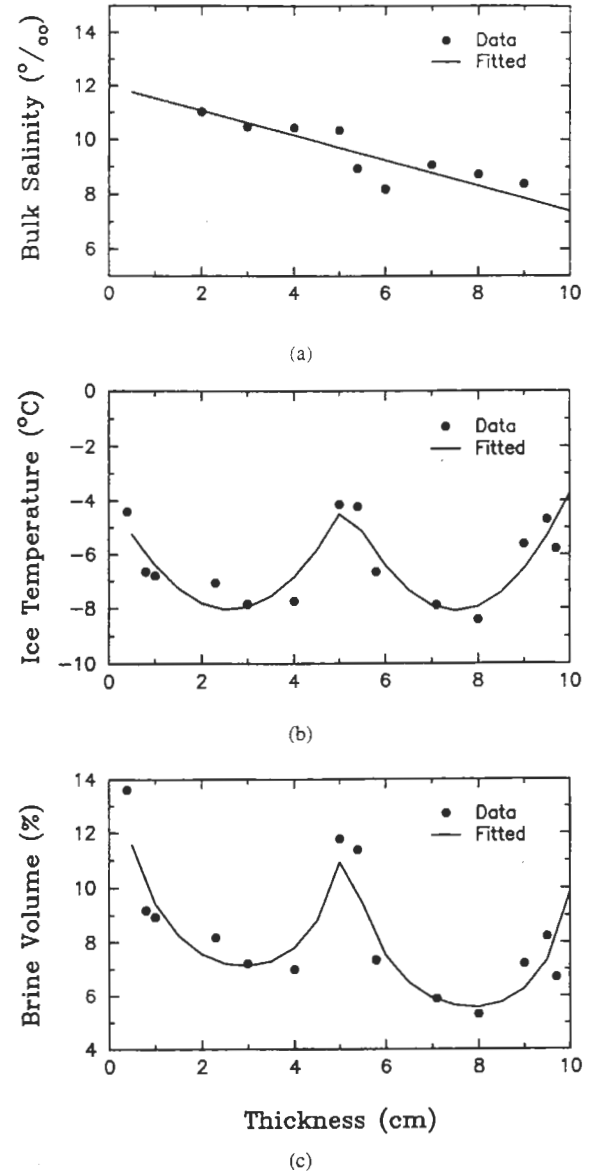


Fig. 7. Bulk properties of the ice sheet as functions of thickness for all growth stages in 2 diurnal cycles: (a) the top panel is for bulk salinity, (b) the middle panel for average ice temperature, and (c) the bottom panel for fractional brine volume.

temperatures were as much as 10 K for  $T_{Bh}$  and 6 K for  $T_{Bv}$ . This is consistent with a higher sensitivity of the emission at horizontal polarization to changes in sea ice permittivity compared to that at vertical polarization for  $50^\circ$  incident angle. Thus, the radiometer observations affirm the diurnal response of the ice sheet. We will use the sea ice physical characteristics under thermal cycling effects presented above to calculate and to explain the observed diurnal backscatter signature.

#### IV. DIURNAL BACKSCATTER SIGNATURE

##### A. Observations

The diurnal cycling signature is evident in the C-band backscatter for the horizontal polarization as shown in Fig. 9. Backscatter data for both  $25^\circ$  and  $30^\circ$  incident angles clearly

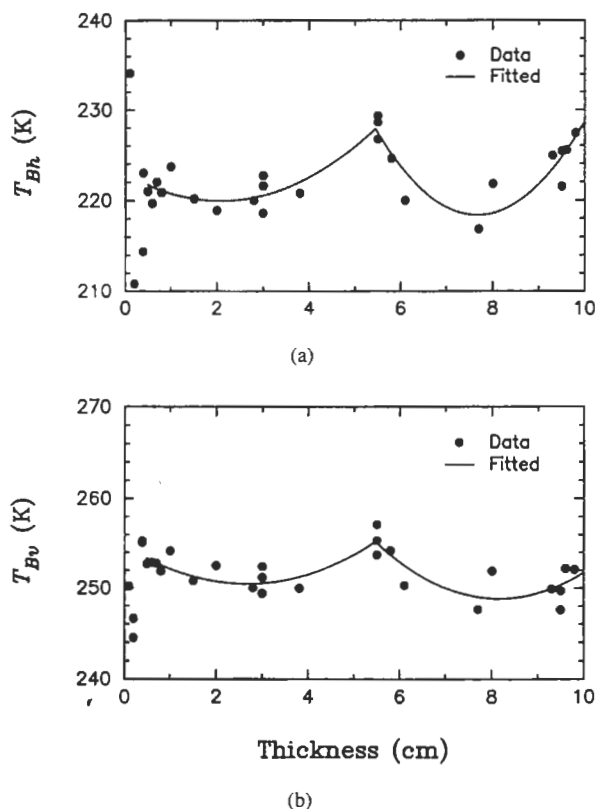


Fig. 8. Brightness temperatures of the sea ice sheet at 90 GHz and 50° incident angle: (a) the top panel is  $T_{Bh}$  for horizontal polarization and (b) the bottom panel is  $T_{Bv}$  for vertical polarization. Symbols are measured data and curves are piecewise quadratic fits for each diurnal thermal cycle. The fits exclude data at early growth stages of 4 mm or less when the phase transition was inhomogeneous and complicated.

exhibit the following characteristics: 1) backscatter diurnal cycles are substantial with variations of 4–6 dB, 2) backscatter and temperature cycles are synchronous and well correlated, and 3) backscatter cycles are repeatable along with diurnal thermal variations. Backscatter at other incident angles and polarizations has a similar diurnal signature as shown later in Fig. 13 in Section IV-D for comparisons between theoretical results and experimental data. For reference, we also present the corresponding measurements of sea ice surface temperature at both ends of the GRF pond in Fig. 9; the temperatures were relatively homogeneous over the entire ice surface considering measurement uncertainties.

Surface salinity measurements and visual inspections indicated that there was no expulsion of brine to the sea ice surface. This agrees with the existence of the incubation layer, which served as a barrier preventing the upward migration of brine to the surface. Thus, the large backscatter change cannot be related to the surface brine expulsion. As shown in Fig. 9, the backscatter peaked at the growth stage of 5.4 cm close to the daytime ice temperature maximum. Fig. 9, however, indicates that the backscatter became less correlated with temperature as the ice sheet grew thicker though the diurnal signature still prevailed. Toward the end of this experiment, more frost flowers appeared on the ice surface especially in the area corresponding to larger incident angles. The cycling

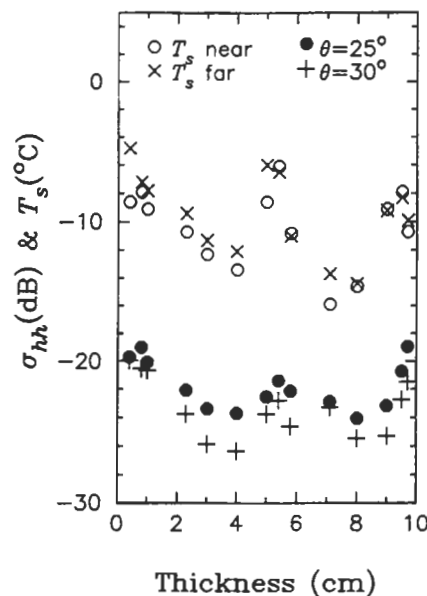


Fig. 9. Observed diurnal cycles in horizontally polarized backscatter for all growth stages with warming and cooling cycles shown in ice surface temperatures. For backscatter, the filled circles are at 25° incident angle and the pluses are at 30° incident angle. For temperatures, the open circles are for data taken with a digital thermometer on the sea ice surface area near the scatterometer area and the crosses are for data obtained with thermistors on the ice surface at the far end of the GRF pond.

of backscatter suggests that the scattering mechanism is related to a reversible process, which is responsive to the diurnal thermal cycling. In the following sections, we will incorporate these experimental observations into a model to relate the backscatter to physical characteristics of sea ice to explain the diurnal cycles in the scatterometer measurements.

### B. Sea Ice Electromagnetic Properties

This section discusses the relationship between sea ice electromagnetic characteristics and physical ice properties undergoing diurnal warming and cooling cycles. Electromagnetic wave propagation, attenuation, reflection, and transmission depend on relative permittivities of the constituents in the inhomogeneous sea ice medium. For the ice background in the sea ice sheet, both the real part [21] and the imaginary part [22] of the permittivity depend on ice temperature. At C band, the permittivity of brine inclusions in the sea ice sheet is also a function of temperature especially for the real part [23]. Thus, diurnal thermal cycles cause corresponding cycles in the effective permittivity of sea ice, which is a mixture of the background ice and brine inclusions.

Scattering from inhomogeneities such as brine inclusions depends on brine volume [24]–[27]. As shown in Fig. 7, the fractional volume of brine inclusions follows the diurnal cycles with a slightly decreasing trend due to desalination. Warming and cooling of the sea ice sheet gives rise to enlargement and shrinkage of brine pockets [28] by melting and freezing of brine pocket walls to maintain the phase distribution on the eutectic curve. For millimeter and submillimeter brine scatterers that are much smaller than the wavelength of 60 mm at 5 GHz, the backscattering cross section in the Rayleigh



regime varies with the sixth power of the scatterer size [29]. Also at 5 GHz, the real part of the permittivity in a brine pocket is larger at a higher temperature [23] resulting in a larger permittivity contrast with the surrounding ice and a stronger scattering effect from an individual brine inclusion. These processes are reversible with diurnal temperature variations and contribute significantly to corresponding diurnal changes in backscatter. However, effects on backscatter caused by thermal diurnal cycling in permittivity, brine volume, and scatterer size are competitive. While increases in brine pocket size and real part of brine permittivity at a higher temperature lead to an increase in backscatter, sea ice effective permittivity also increases [30] and so do attenuation and reflectivity, which act to decrease the backscatter from the sea ice layer.

Surface roughness at the air-ice interface also affects the backscatter diurnal cycles especially at small incident angles. For a given roughness, a higher permittivity in the surface layer increases the surface scattering from sea ice [25] with a weak temperature dependence. In fact, we observed some small scale roughness on the surface of the ice sheet during the ice growth. There was no significant change in the roughness as the ice aged because the surface was frozen solid without wind and wave actions. The appearance of some more frost flowers toward the end of the experiment could increase the roughness. However, this effect is not significant otherwise there should be a general increasing trend in the backscatter, which is not observed in the backscatter measurements. For the highly saline thin ice under consideration, the scattering contribution at C band from the lower interface between ice and water is not important as proved experimentally [11].

### C. Diurnal Backscatter Model

Understanding the impact of diurnal thermal cycles on ice physical properties and consequently on electromagnetic characteristics is necessary for the development of sea ice scattering models to explain the observed diurnal backscatter signature. Such models need to account for the contributive and competitive effects of the scattering mechanisms as discussed in the previous section. We have developed sea ice models including scattering from inhomogeneities in the ice layer, composite roughnesses on medium interfaces, multiple wave interactions with layer boundaries, and wave propagation and attenuation in complex heterogeneous media [24]–[27], [30]. These models encompass physical, structural, thermodynamic, and electrodynamic properties of sea ice. In this section, we review the theory and present the application for a diurnal backscatter model of sea ice.

Fig. 10 represents the scattering configuration of the layered sea ice model. The upper half space is air with permittivity  $\epsilon_0$ . The sea ice layer contains ice with random brine inclusions and has a rough surface at the air-ice interface and brine inclusions in the ice layer. The bottom boundary between ice and water makes little contribution in the backscatter and is modeled as a planar interface. The lower half space is sea water with permittivity  $\epsilon_2$  given by Klein and Swift [31]. The notations in this model for the media are subscript 0 for air, 1 for sea ice, and 2 for sea water.

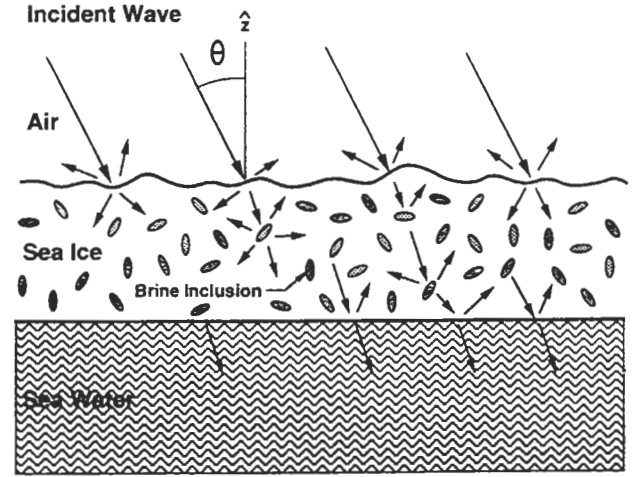


Fig. 10. Scattering configuration of the composite inhomogeneous layered model for diurnal backscatter from sea ice.

For a target area  $A$  at a distance  $r$  from the scatterometer, polarimetric backscattering coefficient  $\sigma_{\mu\tau\nu\kappa}$  is

$$\sigma_{\mu\tau\nu\kappa} = \lim_{\substack{r \rightarrow \infty \\ A \rightarrow \infty}} \frac{4\pi r^2}{A} \frac{\langle E_{\mu s} E_{\nu s}^* \rangle}{E_{\tau i} E_{\kappa i}^*} \quad (1)$$

where  $E$  is an electric field with its complex conjugate represented with an asterisk, the angular brackets denote the ensemble average, subscripts  $\mu$ ,  $\nu$ ,  $\tau$ , and  $\kappa$  are  $h$  for horizontal or  $v$  for vertical polarization, and  $i$  and  $s$  for incident and scattered fields, respectively.

For scatterers such as brine inclusions in the sea ice sheet, the ensemble average in (1) is determined by

$$\begin{aligned} \langle \bar{E}_s(\bar{r}) \cdot \bar{E}_s^*(\bar{r}) \rangle &= \sum_{i,j,k,l,m}^{x,y,z} k_0^4 \int_0^\pi d\psi_{1f} \int_0^{2\pi} d\phi_{1f} \\ &\quad \cdot p_1(\psi_{1f}, \phi_{1f}) \int_{V_1} d\bar{r}_1 \int_{V_1} d\bar{r}_1^o \\ &\quad \cdot C_{1\xi jklm}(\bar{r}_1, \bar{r}_1^o; \psi_{1f}, \phi_{1f}) \\ &\quad \cdot [\langle G_{01ij}(\bar{r}, \bar{r}_1) \rangle \langle F_{1k}(\bar{r}_1) \rangle] \\ &\quad \cdot [\langle G_{01il}(\bar{r}, \bar{r}_1^o) \rangle \langle F_{1m}(\bar{r}_1^o) \rangle]^* \end{aligned} \quad (2)$$

where  $k_0$  is the free-space wave number,  $p_1$  is the scatterer orientation distribution with Eulerian angles  $\psi_{1f}$  and  $\phi_{1f}$ , position  $\bar{r}_1$  or  $\bar{r}_1^o$  is in volume  $V_1$  of the sea ice sheet,  $\langle G \rangle$  is for the mean dyadic Green's function, and  $\langle F \rangle$  is the mean incident field. As seen in the vertical thin section in Fig. 5 and other ice samples, the ice crystallographic  $c$ -axes are tilted with no preferential azimuthal orientation. Thus, we describe the orientation distribution with  $p_1 = \sin \psi_{1f} / (4\pi)$  for random orientation.

In (1), correlation function  $C_{1\xi jklm}$  of the scatterer is [25]

$$\begin{aligned} C_{1\xi jklm}(\bar{r}_1, \bar{r}_1^o; \psi_{1f}, \phi_{1f}) \\ = \int_{-\infty}^{\infty} d\bar{\beta} \Gamma_{1jklm} \Phi_{1\xi}(\bar{\beta}) e^{-i\bar{\beta} \cdot (\bar{r}_1 - \bar{r}_1^o)} \end{aligned} \quad (3)$$

where  $\Phi_{1\xi}$  is the normalized correlation function defined in the local coordinates  $(x', y', z')$  as [24]

$$\Phi_{1\xi}(\bar{k}') = \frac{\ell_{x'}\ell_{y'}\ell_{z'}}{\pi^2(1 + k_x'^2\ell_{x'}^2 + k_y'^2\ell_{y'}^2 + k_z'^2\ell_{z'}^2)} \quad (4)$$

in which  $\ell_{x'}$ ,  $\ell_{y'}$ , and  $\ell_{z'}$  are three different correlation lengths for an ellipsoidal scatterer in the local coordinates  $(x', y', z')$  related to  $(x, y, z)$  by Eulerian angles  $\psi_{1f}$  and  $\phi_{1f}$ . The variance  $\Gamma_{1jklm}$  of permittivity fluctuations in the correlation function relates to the brine volume fraction in the sea ice sheet. The dependence of the brine volume on diurnal cycles governed by the thermodynamic phase equilibrium thereby contributes to the backscatter diurnal variations.

While giving rise to the backscattering, brine inclusions also influence electromagnetic wave propagation and attenuation characterized with effective permittivity  $\epsilon_{1\text{eff}}$ . For sea ice with randomly oriented brine pockets, the effective permittivity is isotropic and expressed as

$$\epsilon_{1\text{eff}} = \epsilon_{1g} + \epsilon_0 [1 - \xi_{1\text{eff}} \langle S_1 \rangle]^{-1} \xi_{1\text{eff}} \quad (5)$$

where  $\langle S_1 \rangle$  is the average of the polarizability of ellipsoidal brine inclusions [25]. The term  $\epsilon_{1g}$  in (5) represents the quasistatic effect, which has the form of the Polder–van Santen mixing formula and relates to permittivities of the constituents in sea ice. Thus, diurnal thermal effects on permittivities of the ice background and brine inclusions are present even in the zeroth-order dielectric mixing. Effective scatterer  $\xi_{1\text{eff}}$  accounts for scattering effects on wave propagation and attenuation. The same form of correlation function shown above also characterizes  $\xi_{1\text{eff}}$ ; therefore, it directly varies with the diurnal cycles in brine volume and scatterer size. This incorporates into the model the competitive effect in scattering mechanisms as discussed in Section IV-B.

For rough surface scattering in layered media, we have developed and presented the model [26]. The surface scattering is a function of wave vector; thus, this mechanism is less sensitive to the diurnal effect since the wave number depends only on the complex square root of the diurnally cycled permittivity. We have presented complete and explicit mathematical expressions for the composite scattering including volume and surface mechanisms and for effective permittivity of sea ice elsewhere [24]–[27], [30].

#### D. Data Comparisons

The model requires permittivities of ice background and brine inclusions in the inhomogeneous sea ice sheet. Empirical functions of these temperature-dependent permittivities are available in given references as discussed in Section IV-B. With measured temperatures, these functions determine variations in the model input permittivities under effects of diurnal thermal cycles. Another important input is the brine volume, which clearly shows the warming and cooling effects as seen in Fig. 7. For the rough surface, we use a height standard deviation of 0.65 mm and a correlation length of 2.5 cm to model the frozen solid ice surface for all growth stages. In this case, variations in the effective permittivity of sea ice contribute to the diurnal signature in the surface scattering.

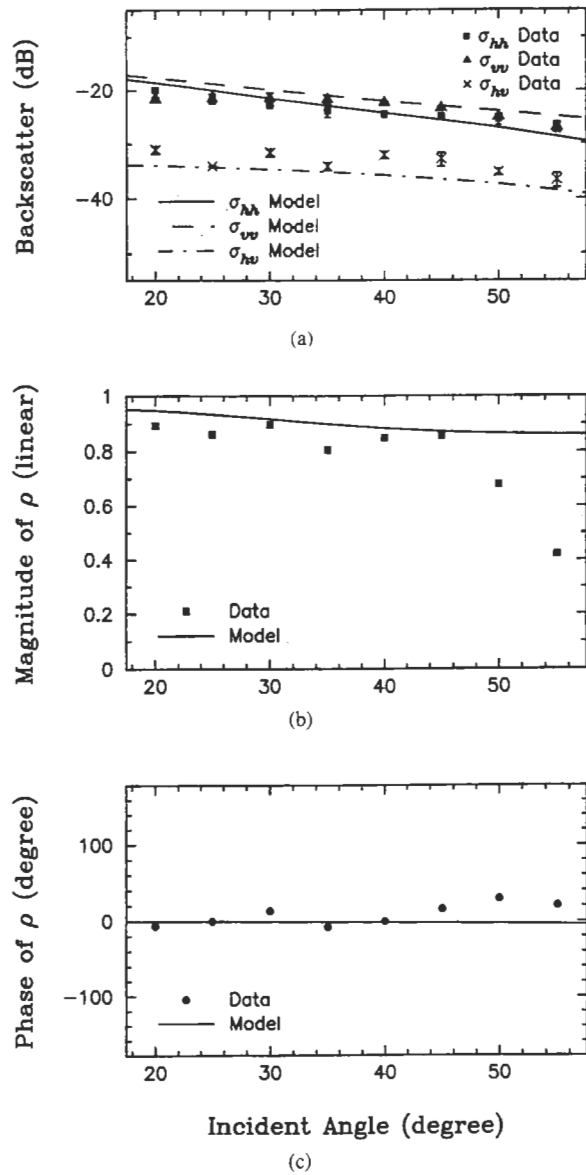


Fig. 11. Comparison of polarimetric backscatter data and model calculations as functions of incident angle for the intermediate growth stage at 5.4-cm thick ice: (a) The top panel is for backscattering coefficients  $\sigma_{hh}$ ,  $\sigma_{vv}$ ,  $\sigma_{hv}$ , and (b) the middle panel for magnitude of complex correlation coefficient  $\rho$  between horizontal and vertical returns, and (c) the bottom panel for phase of  $\rho$ .

For brine inclusions, the correlation lengths are  $\ell_{1y'} = 0.05$  mm and  $\ell_{1x'} = \ell_{1z'}/2 = 1$  mm. We obtain these parameters by matching the backscatter data at the growth stage corresponding to the ice thickness of 3 cm. The change in brine volume at other growth stages then determines the pocket brine size and thus the correlation lengths with the same axial ratios for all cases. With this approach, measured temperature and salinity govern all the model parameters for all growth stages without allowing any extraneous change in these parameters. Constrained by the sea ice thermodynamics and electrodynamics, backscatter calculated from the model needs to reproduce and to explain the diurnal warming and cooling cycles exhibited in the backscatter signature measured by the scatterometer.

Fig. 11 compares calculated and measured polarimetric backscatter as a function of incident angles from 20 to

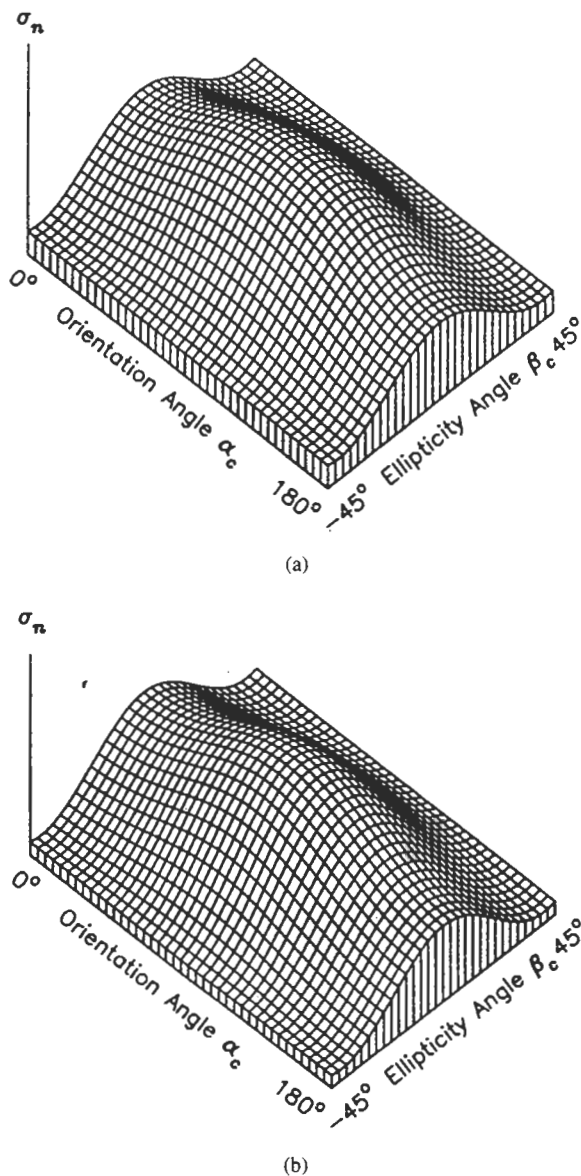


Fig. 12. Comparison of polarization signatures of sea ice versus polarization orientation and ellipticity angles at  $40^\circ$  incident angle for the intermediate growth stage at 5.4-cm thick ice: (a) polarization signature from measured data and (b) polarization signature from model results.

$55^\circ$  for the intermediate growth stage corresponding to 5.4-cm-thick ice. In general, backscattering coefficients  $\sigma_{hh}$  and  $\sigma_{vv}$  compare well. However, theoretical cross-polarized backscatter  $\sigma_{hv}$  is lower than the experimental data. This is because more complicated structures in sea ice and higher order scattering are not considered in the model. For the complex correlation coefficient  $\rho$ , the model magnitude is slightly higher than experimental data; both calculated and measured phases are small for most incident angles. At large incident angles such as  $50^\circ$  and  $55^\circ$ , measured magnitudes of  $\rho$  are much lower and phases of  $\rho$  are higher than the calculated ones. On the ice surface at these incident angles, some frost flowers appeared at this growth stage, which are not included in the model.

Polarization signatures, which are normalized backscatter  $\sigma_n$  at all polarizations including linear, circular, and elliptical

waves [24], are plotted as a function of orientation and ellipticity angles in Fig. 12 for the 5.4-cm-thick ice at  $40^\circ$  incident angle. The computed and measured polarization signatures have the same shape as observed in Fig. 12. Both polarization signatures peak in the middle where orientation angle  $\alpha_c$  is  $90^\circ$  and ellipticity angle  $\beta_c$  is  $0^\circ$ , indicating that the vertical linear polarization gives a maximum return above all possible polarization states. The pedestal in the calculated signature, however, is lower implying a lower depolarizing effect in the theory as compared to the measured results.

Fig. 13 shows comparisons of backscatter signatures between theory and experiment at incident angles from  $25^\circ$  to  $50^\circ$  for the two diurnal cycles. All incident angles have higher backscatter during the warm daytime and lower backscatter during nighttime. While absolute backscatter is larger at the small incident angle of  $25^\circ$ , diurnal variations at this angle are smaller compared to variations at larger incident angles. Overall, theoretical backscatter follows the diurnal cycling trends in the experimental data. Calculated values and measured data for copolarized backscatter  $\sigma_{hh}$  and  $\sigma_{vv}$  are in fair agreement. An exception is the high measured backscatter at  $35^\circ$ – $50^\circ$  corresponding to 7.1-cm-thick ice, which in this particular case could be caused by effects from the side of the GRF pond when the antenna was turned too much in azimuth toward the concrete edge of the pond. Calculated cross-polarized returns are lower than measured data which have large fluctuations and the diurnal cycles are not well defined. In general, the model based on physical properties of sea ice undergoing diurnal warming and cooling cycles captures the diurnal cycling effects as observed in the measurements.

## V. SUMMARY

We successfully carried out an experiment at the Geophysical Research Facility in the Cold Regions Research and Engineering Laboratory to study diurnal thermal cycling effects on microwave signatures of thin sea ice. The ice sheet grew from open water with a salt mixture similar to sea water to a thickness of 10 cm in 2.5 days extending over two diurnal cycles. During the ice growth, we measured polarimetric backscatter with the Jet Propulsion Laboratory polarimetric scatterometer at C band, in conjunction with microwave brightness temperature measurements, sea ice characterization, and environmental monitoring.

Throughout this experiment, the temperature conditions closely simulated those of the Arctic early spring with a low of  $-36^\circ\text{C}$  during the nighttime and the daytime high of only  $-12^\circ\text{C}$ . The amplitude of midlatitude winter solar radiation was also similar to the Arctic condition. Together with a calm atmosphere, these conditions were particularly suitable for the study of the diurnal signature on backscatter from the sea ice sheet. Correlated with the insolation cycles, ice temperature, brine volume, growth rate, thickness, and millimeter-wave brightness temperatures showed diurnal cycles with a lag of approximately 2.5 h from the short-wave radiation peak at solar noon.

Experimental measurements reveal repeatable diurnal cycles in backscatter, which are synchronous and well correlated with

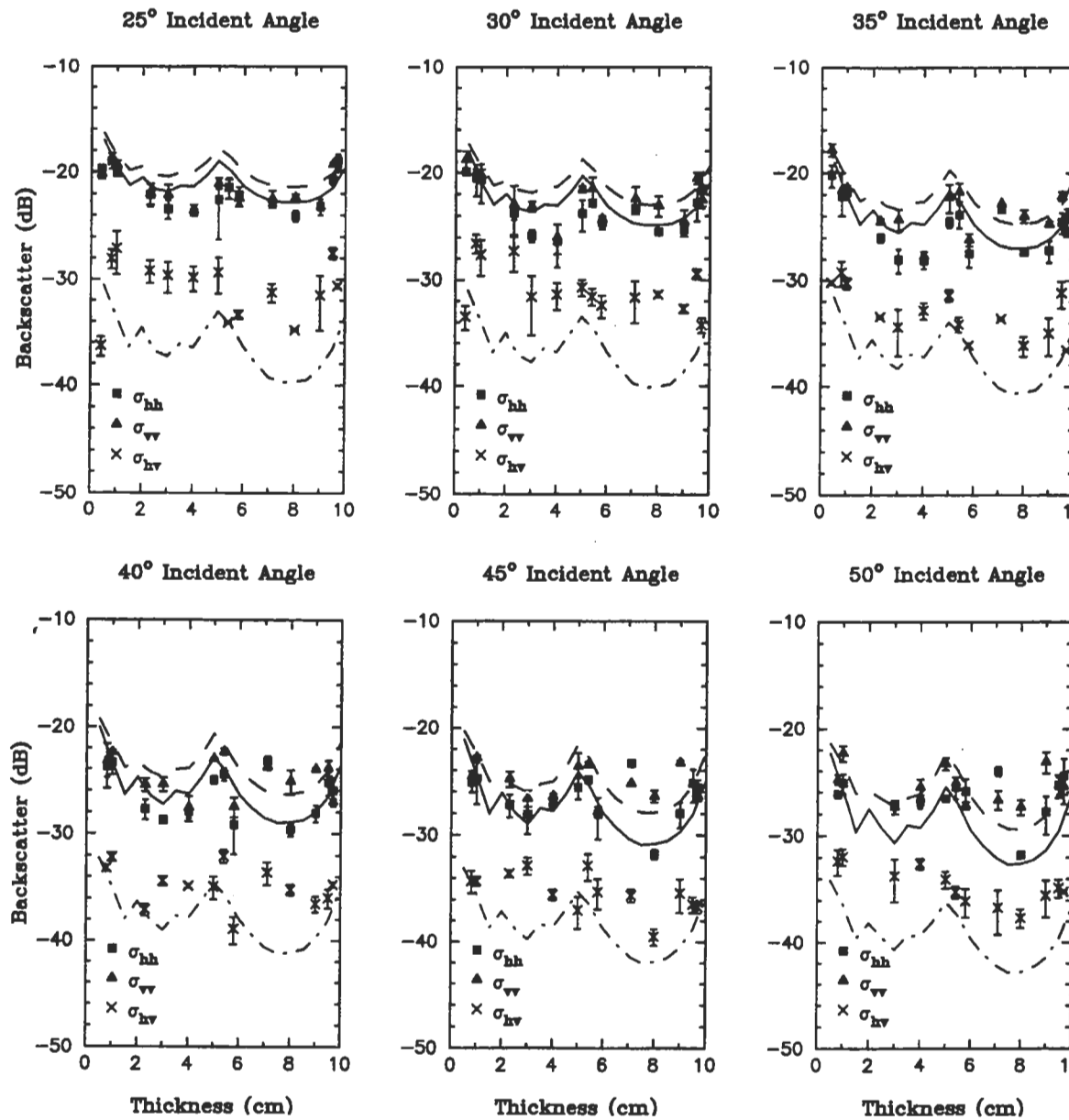


Fig. 13. Comparisons of measured and calculated backscatter for all growth stages in two diurnal thermal cycles for incident angles at 25, 30, 35, 40, 45, and 50°. For measurements, squares represent  $\sigma_{hh}$ , triangles are  $\sigma_{vv}$ , and crosses are  $\sigma_{hv}$ . For calculations, continuous, dashed, and dash-dotted curves represent  $\sigma_{hh}$ ,  $\sigma_{vv}$ , and  $\sigma_{hv}$ , respectively.

the cycles in sea ice physical parameters. The backscatter diurnal variations were substantial with changes of 4–6 dB between day and night. We use a diurnal sea ice backscatter model based on thermal and electromagnetic properties of sea ice to calculate backscatter and to explain the diurnal cycling trend in experimental observations. The composite model, incorporating both volume and surface interactions, accounts for contributive as well as competitive effects in the scattering mechanisms due to diurnal variations in physical parameters of sea ice. Calculations for copolarized backscatter compare well with experimental data. Theoretical cross-polarized backscatter is lower than the measurements because the theory does not include complicated conditions such as frost flowers on the surface of the ice sheet and ignores higher order scattering. Since this work is focused on backscatter at C band for all

polarizations, it is useful for application to spaceborne radars such as ERS, ENVISAT, and RADARSAT operating at C-band with different polarizations.

The important implication of the results in this paper is that the substantial diurnal variations in backscatter should be included in inversion algorithms for retrieving sea ice geophysical parameters from satellite SAR and scatterometer data. This is particularly relevant to sun synchronous satellites which acquire data along ascending and descending orbit paths at daytimes and nighttimes over the same area.

#### ACKNOWLEDGMENT

The assistance of J. Govoni and B. Elder in the experiment is gratefully acknowledged.

## REFERENCES

- [1] G. A. Maykut, "Energy exchange over young sea ice in the central Arctic," *J. Geophys. Res.*, vol. 83, no. C7, pp. 3646–3658, 1978.
- [2] ———, "Large-scale heat exchange and ice production in the central Arctic," *J. Geophys. Res.*, vol. 87, no. C10, pp. 7971–7984, 1982.
- [3] D. Ruffieux, P. O. G. Persson, C. W. Fairall, and D. E. Wolfe, "Ice pack and lead surface energy budgets during LEADDEX 1992," *J. Geophys. Res.*, vol. 100, no. C3, pp. 4953–4612, 1995.
- [4] M. G. McPhee and T. P. Stanton, "Turbulence in the statically unstable oceanic boundary layer under Arctic leads," *J. Geophys. Res.*, vol. 101, no. C3, pp. 6409–6428, 1996.
- [5] LeadEx Group, "The LeadEx experiment," *EOS Trans. AGU*, vol. 74, no. 35, p. 393, 1993.
- [6] M. Ikeda, "Snow cover detected by diurnal warming of sea ice/snow surface off Labrador in NOAA imagery," *IEEE Trans. Geosci. Remote Sensing*, vol. 27, pp. 552–560, Sept. 1989.
- [7] D. G. Barber, E. F. LeDrew, D. G. Flett, M. Shokr, and J. Falkingham, "Seasonal and diurnal variations in SAR signatures of landfast sea ice," *IEEE Trans. Geosci. Remote Sensing*, vol. 30, pp. 638–642, May 1992.
- [8] S. E. Shih, K. H. Ding, S. V. Nghiem, C. C. Hsu, J. A. Kong, and A. K. Jordan, "Thin saline ice thickness retrieval using time series C-band polarimetric radar measurements," *IEEE Trans. Geosci. Remote Sensing*, to be published.
- [9] U.S. Army TECOM Hanover Meteorological Team, "Monthly meteorological data, CRREL test cell," Atmos. Sci. Div., U.S. Army Corps of Engineers, Cold Regions Research and Engineering Laboratory, Hanover, NH, Int. Rep. 1123, 1994.
- [10] S. V. Nghiem, "C-band polarimetric scatterometer: System, operation, sensitivity and calibration," in *Proc. Sea Ice Electromagn. Workshop*, Hanover, NH, Sept. 14–16, 1993.
- [11] S. V. Nghiem, R. Kwok, S. H. Yueh, A. J. Gow, D. K. Perovich, C. C. Hsu, K. H. Ding, and J. A. Kong, "Evolution in polarimetric signatures of thin saline ice under constant growth," *Radio Sci.*, vol. 32, no. 1, pp. 127–151, 1997.
- [12] T. G. Grenfell and A. W. Lohanick, "Temporal variations of the microwave signatures of sea ice during the late spring and early summer near Mould Bay NWT," *J. Geophys. Res.*, vol. 90, no. C3, pp. 5063–5074, 1985.
- [13] C. M. Adams, Jr., D. N. French, and W. D. Kingery, "Solidification of sea ice," *J. Glaciology*, vol. 3, pp. 745–760, 1960.
- [14] G. Neumann and W. J. Pierson, Jr., *Principles of Physical Oceanography*. Englewood Cliffs, NJ: Prentice-Hall, 1966.
- [15] G. A. Maykut and N. Untersteiner, "Some results from a time dependent, thermodynamic model of sea ice," *J. Geophys. Res.*, vol. 76, no. 6, pp. 1550–1575, 1971.
- [16] A. J. Gow, "Crystalline structure of urea ice sheets used in modeling experiments in the CRREL test basin," U.S. Army Corps of Engineers, Cold Regions Research and Engineering Laboratory, Hanover, NH, Rep. 84-24, 1984.
- [17] A. J. Gow, W. F. Weeks, P. Kosloff, and S. Carsey, "Petrographic and salinity characteristics of brackish water ice in the Bay of Bothnia," U.S. Army Corps of Engineers, Cold Regions Research and Engineering Laboratory, Hanover, NH, Rep. 92-13, 1992.
- [18] W. F. Weeks and S. F. Ackley, *The Growth, Structure, and Properties of Sea Ice*, U.S. Army Corps of Engineers, Cold Regions Research and Engineering Laboratory, Hanover, NH, 1982, Monograph Series vol. 82-1.
- [19] M. Nakawo and N. K. Sinha, "A note on brine layer spacing of first-year sea ice," *Atmos. Ocean*, vol. 22, no. 2, pp. 193–206, 1984.
- [20] G. F. N. Cox and W. F. Weeks, "Equations for determining the gas and brine volumes in sea-ice samples," *J. Glaciology*, vol. 29, no. 12, pp. 306–316, 1983.
- [21] M. R. Vant, R. O. Ramseier, and V. Makios, "The complex-dielectric constant of sea ice at frequencies in the range 0.1–40 GHz," *J. Appl. Phys.*, vol. 49, no. 3, pp. 1264–1280, 1978.
- [22] M. E. Tiuri, A. H. Sihvola, E. G. Nyfors, and M. T. Hallikainen, "The complex dielectric constant of snow at microwave frequencies," *IEEE J. Ocean. Eng.*, vol. OE-9, no. 5, pp. 377–382, 1984.
- [23] A. Stogryn and G. J. Desargant, "The dielectric properties of brine in sea ice at microwave frequencies," *IEEE Trans. Antennas Propagat.*, vol. AP-33, no. 5, pp. 523–532, 1985.
- [24] S. V. Nghiem, R. Kwok, J. A. Kong, and R. T. Shin, "A model with ellipsoidal scatterers for polarimetric remote sensing of anisotropic layered media," *Radio Sci.*, vol. 28, no. 5, pp. 687–703, 1993.
- [25] S. V. Nghiem, R. Kwok, S. H. Yueh, J. A. Kong, M. A. Tassoudji, C. C. Hsu, and R. T. Shin, "Polarimetric scattering from layered media with multiple species of scatterers," *Radio Sci.*, vol. 30, no. 4, pp. 835–852, 1995.
- [26] S. V. Nghiem, R. Kwok, S. H. Yueh, and M. R. Drinkwater, "Polarimetric signatures of sea ice. 1. Theoretical model," *J. Geophys. Res.*, vol. 100, no. C7, pp. 13665–13679, 1995.
- [27] ———, "Polarimetric signatures of sea ice. 2. Experimental observations," *J. Geophys. Res.*, vol. 100, no. C7, pp. 13 681–13 698, 1995.
- [28] D. K. Perovich and A. J. Gow, "A statistical description of microstructure of young ice," *J. Geophys. Res.*, vol. 96, no. C9, pp. 16 943–16 953, 1991.
- [29] J. A. Kong, *Electromagnetic Wave Theory*. New York: Wiley, 1986.
- [30] S. V. Nghiem, R. Kwok, J. A. Kong, R. T. Shin, S. A. Arcone, and A. J. Gow, "An electrothermodynamic model with distributed properties for effective permittivities of sea ice," *Radio Sci.*, vol. 31, no. 2, pp. 297–311, 1996.
- [31] L. A. Klein and C. Swift, "An improved model for the dielectric constant of sea water at microwave frequencies," *IEEE Trans. Antennas Propagat.*, vol. AP-25, pp. 104–111, Jan. 1977.



**Son V. Nghiem** (M'86) received the B.S. degree in electrical engineering (summa cum laude) in 1985 from Texas A & M University, College Station. He received the S.M. degree in 1988 and the Ph.D. degree in 1991, both from the Department of Electrical Engineering and Computer Science, Massachusetts Institute of Technology, Cambridge.

In 1991, he joined the Jet Propulsion Laboratory, California Institute of Technology, Pasadena, where he is a Technical Task Manager with the Defense Space Technology, Center for Space Microelectronics Technology, Technology and Applications Programs. His research encompasses active and passive remote sensing techniques, instrumentation, and experimentation, electromagnetic wave theory and applications, and modeling of geophysical environment with consideration of physiological and morphological processes.

Dr. Nghiem is a Member of the American Geophysical Union, the Scientific Research Society of Sigma Xi, and the Honor Society of Phi Kappa Phi.

**Ronald Kwok** (S'82–M'84), for photograph and biography, see this issue, p. 37.



**Simon H. Yueh** (M'92) received the S.B. and S.M. degrees in 1982 and 1984, respectively, from the Electrical Engineering Department, National Taiwan University, Taipei, R.O.C., and the Ph.D. degree in electrical engineering in 1991 from the Massachusetts Institute of Technology (MIT), Cambridge.

He was a Postdoctoral Research Associate at MIT from February to August 1991. He developed various techniques for the calibration of polarimetric radars and theoretical models for the remote sensing of rough surfaces and random media. In 1991, he joined the SAR Systems Development and Processing Group at the Jet Propulsion Laboratory, California Institute of Technology, Pasadena. He has developed airborne polarimetric radiometers for ocean remote sensing and conducted aircraft scatterometer and radiometer experiments demonstrating the sensitivity of polarimetric brightness temperatures to ocean surface wind vectors. His current fields of interest include techniques and microwave instrumentation for remote sensing of ocean winds and polar ice, theories for active and passive microwave remote sensing, and applications of interferometric and polarimetric SAR data.

Dr. Yueh received the 1995 IEEE Geoscience and Remote Sensing Society Transaction Prize Paper award for his work on polarimetric radiometry.



**Anthony J. Gow** received the M.Sc. and D.Sc. degrees in geology in 1965 and 1975, respectively, from Victoria University, Wellington, New Zealand.

He is currently a Geologist with the U.S. Army Cold Regions Research and Engineering Laboratory, Hanover, NH. His long-term interests have included studies of the structural, paleoclimate, and physical properties of Antarctic snow and ice. Most recently, he was a member of the U.S. research team investigating the paleoclimate implications of an ice core that penetrated 3053 m to bedrock in Central

Greenland. He has also been involved for a number of years in studies of the crystalline structure and physical properties of lake, river, and sea ice and has extended these studies to laboratory-grown model ices. Since 1985, he has been Adjunct Professor of Glaciology in the Earth Sciences Department at the University of New Hampshire, Manchester.

Dr. Gow is a member of the American Geophysical Union, the International Glaciological Society, and the Antarctic Society.



**Donald K. Perovich** received the M.S. and Ph.D. degrees in geophysics in 1979 and 1983, respectively, from the University of Washington, Seattle.

He is currently a Geophysicist with the U.S. Army Cold Regions Research and Engineering Laboratory, Hanover, NH. His long-term interests include sea ice optical properties and thermodynamics. Recently, he has been involved in an interdisciplinary program investigating the electromagnetic properties of sea ice. During this program, he studied the reflection and transmission of solar radiation by sea

ice and developed statistical descriptions of sea ice microstructure.

Dr. Perovich is a member of the American Geophysical Union and the International Glaciological Society.



**Chih-Chien Hsu** received the B.S.E.E. degree from the National Chiao Tung University, Hsinchu, Taiwan, R.O.C., in 1987 and the M.S.E.E. and Ph.D. degrees from the Massachusetts Institute of Technology (MIT), Cambridge, in 1992 and 1996, respectively.

While at MIT, he worked on various remote sensing research projects as a Research Assistant. He is now with Hughes Space and Communications Company.

**Kung-Hau Ding** received the B.S. degree from the National Tsing-Hua University, Hsinchu, Taiwan, R.O.C., the M.S. degree in physics and electrical engineering, and the Ph.D. degree in electrical engineering from the University of Washington, Seattle.

From 1989 to 1993, he was with the Physical Science Laboratory, New Mexico State University, Las Cruces. In October 1993, he joined the Research Laboratory of Electronics, Massachusetts Institute of Technology, Cambridge. His research interests are wave propagation and scattering in random media and remote sensing.

**Jin Au Kong** (S'65-M'69-SM'74-F'85), for photograph and biography, see this issue, p. 83.



**Thomas C. Grenfell** (M'94) received the Sc.B. degree from Brown University, Providence, RI, in 1965, the M.S. degree from the University of Chicago, Chicago, IL, in 1968, and the Ph.D. degree from the University of Washington, Seattle, in 1972.

He has been a Research Professor at the University of Washington since 1991, specializing in observations and theoretical modeling of the structural and electromagnetic properties of sea ice and snow.

Dr. Grenfell is currently a Finance Chairman of IGARSS'98.